Supplementary Information for Tuning light-matter interaction of near-infrared nanoplasmonic scintillators

Michał Makowski[1,2,*], **Dominik Kowal**[1], **and Muhammad Danang Birowosuto**[1]

[1]Łukasiewicz Research Network - PORT Polish Center for Technology Development, Wrocław, 54-066, Poland
[2]Institute of Physics, Faculty of Physics, Astronomy and Informatics, Nicolaus Copernicus University, Grudziadzka 5, 87-100 Torun, Poland
[*]michal.makowski@port.lukasiewicz.gov.pl

ABSTRACT

List of Figures

List of Tables

Quantum-optical model and numerical implementation

The emitter-antenna system was modeled within the framework of open quantum systems using a driven-dissipative Jaynes-Cummings formalism[1–3]. The emitter was treated as an effective two-level system coupled to a single confined optical mode representing the plasmonic antenna. In the rotating frame used in the simulations, the Hamiltonian was written as

$$\hat{H} = \hbar\Delta_c \hat{a}^\dagger \hat{a} + \hbar g \left(\hat{a}^\dagger \hat{\sigma} + \hat{a}\hat{\sigma}^\dagger\right), \tag{S1}$$

where $\hat{a}$ and $\hat{a}^\dagger$ denote the annihilation and creation operators of the antenna mode, $\hat{\sigma}$ and $\hat{\sigma}^\dagger$ are the lowering and raising operators of the emitter, $\hat{\sigma}_z$ is the Pauli z operator of the emitter, g is the light-matter coupling strength, and $\Delta_c = \omega_c - \omega_e$ is the detuning between the antenna and emitter transition energies.

The system dynamics were described by the Lindblad master equation

$$\frac{d\hat{\rho}}{dt} = -\frac{i}{\hbar}[\hat{H}, \hat{\rho}] + \sum_i \mathscr{L}_i[\hat{\rho}], \tag{S2}$$

where $\hat{\rho}$ is the density matrix and the Lindblad superoperators account for antenna loss, emitter decay, pure dephasing, and incoherent pumping. Each dissipative channel was introduced in the standard Lindblad form

$$\mathscr{L}_{\hat{C}}[\hat{\rho}] = \hat{C}\hat{\rho}\hat{C}^\dagger - \frac{1}{2}\left(\hat{C}^\dagger\hat{C}\hat{\rho} + \hat{\rho}\hat{C}^\dagger\hat{C}\right), \tag{S3}$$

where $\hat{C}$ denotes the corresponding collapse operator. In the numerical implementation, the collapse operators were taken as

$$\sqrt{\kappa}\,\hat{a}, \qquad \sqrt{\gamma}\,\hat{\sigma}, \qquad \sqrt{\gamma_\phi/4}\,\hat{\sigma}_z, \qquad \sqrt{P_c}\,\hat{a}^\dagger, \qquad \sqrt{P_x}\,\hat{\sigma}^\dagger, \tag{S4}$$

where κ is the antenna loss rate, γ is the emitter radiative decay rate, γ_ϕ is the pure dephasing rate, and P_c and P_x are the incoherent pumping rates of the antenna and emitter channels, respectively. In practice, only operators corresponding to non-zero rates were included in the simulations.

With this choice of collapse operators, the decay of emitter coherence is governed by the transverse relaxation rate

$$\Gamma_2 = \frac{\gamma}{2} + \gamma_\phi. \tag{S5}$$

Accordingly, the effective homogeneous linewidth of the emitter is determined not only by the radiative decay rate γ, but by the combined contribution of population decay and pure dephasing. In the parameter regimes considered here, the emitter linewidth was therefore controlled predominantly by γ_ϕ whenever $\gamma \ll \gamma_\phi$.

The steady-state density matrix $\hat{\rho}_{ss}$, defined by the condition

$$\frac{d\hat{\rho}_{ss}}{dt} = 0, \tag{S6}$$

was obtained numerically and used as the reference state for the evaluation of temporal and spectral observables. The temporal response was analyzed through the first-order correlation function of the detected field,

$$G^{(1)}(\tau) = \langle \hat{E}^\dagger_{det}(\tau)\hat{E}_{det}(0)\rangle_{ss}, \tag{S7}$$

where the subscript ss denotes averaging in the steady state. The detected field operator was defined as

$$\hat{E}_{det} = \sqrt{F_{antenna}\kappa}\,\hat{a} + \sqrt{F_{rad}\gamma}\,\hat{\sigma}, \tag{S8}$$

with $F_{antenna}$ and F_{rad} representing the relative weights of the antenna-like and emitter-like detection channels. For visualization, the calculated temporal correlation was normalized to its zero-delay magnitude, and a global phase rotation was applied so that the plotted traces represent the real, imaginary, or absolute parts of the normalized first-order coherence function.

The spectral response was evaluated from steady-state two-time correlation functions using the standard quantum-optical relation between emission spectra and Fourier-transformed field correlations. In the implementation used here, the frequency variable ω was defined relative to the antenna resonance. The antenna-like contribution was calculated as

$$S_{antenna}(\omega) \propto F_{antenna}\frac{\kappa}{\pi}\,\mathrm{Re}\left[\int_0^\infty \langle \hat{a}^\dagger(\tau)\hat{a}(0)\rangle_{ss} e^{i\omega\tau}\,d\tau\right], \tag{S9}$$

while the emitter-like contribution was written as

$$S_{\mathrm{rad}}(\omega) \propto F_{\mathrm{rad}} \frac{\gamma}{\pi} \mathrm{Re}\left[\int_0^\infty \langle \hat{\sigma}^\dagger(\tau)\hat{\sigma}(0)\rangle_{\mathrm{ss}} e^{i\omega\tau}\, d\tau\right]. \tag{S10}$$

The detected spectrum was then constructed as an incoherent sum of these two channels,

$$S_{\mathrm{det}}(\omega) = S_{\mathrm{antenna}}(\omega) + S_{\mathrm{rad}}(\omega). \tag{S11}$$

Accordingly, the temporal response and the spectral response were not evaluated from exactly the same composite detected-field expression: the first-order temporal correlation was calculated using the mixed detected-field operator $\hat{E}_{\mathrm{det}}$, whereas the detected spectrum was assembled as the sum of separately evaluated antenna-like and emitter-like spectral contributions. In this form, interference terms between the two detection channels were not included explicitly in the spectral decomposition.

All simulations were performed in Python using the QuTiP library[4,5]. The steady-state density matrix was obtained with `qutip.steadystate`, the first-order temporal correlation function was calculated using `correlation_2op_1t`, and the spectra were evaluated with `qutip.spectrum`. The antenna Hilbert space was truncated to a finite number of Fock states, and the numerical solver settings were chosen to ensure convergence of both the temporal correlation functions and the spectra. The temporal axis was expressed in physical time units through the energy-time relation set by $\hbar$.

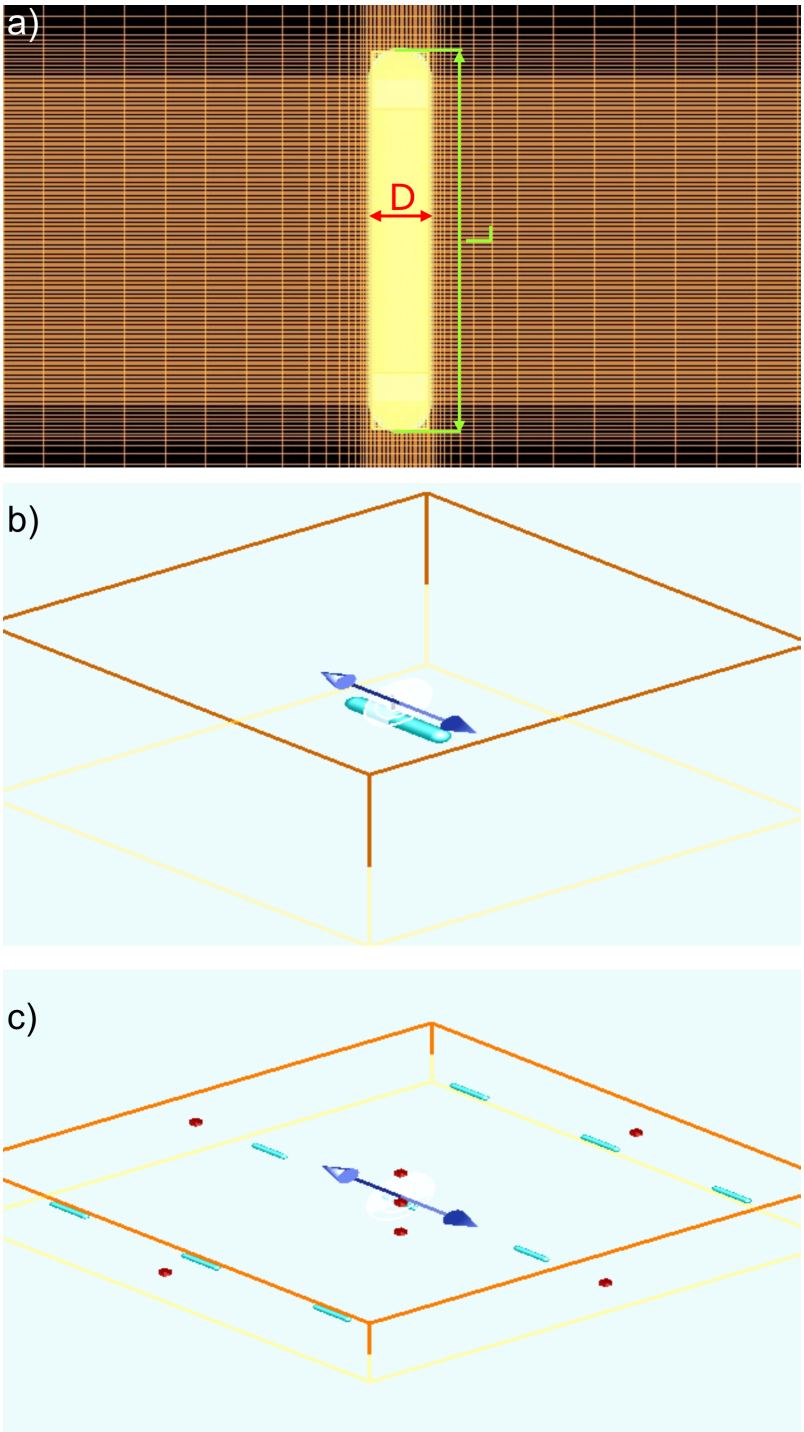

Figure S1. Schematic representation of the simulated Au nanorod structures and excitation geometry. **a**, Single Au nanorod of length *L* and diameter *D*, overlaid with the simulation mesh (orange lines). **b**, Single Au nanorod illuminated by a plane-wave source (gray region). **c**, Periodic Au nanorod array defined by lattice periods *X* and *Y*.

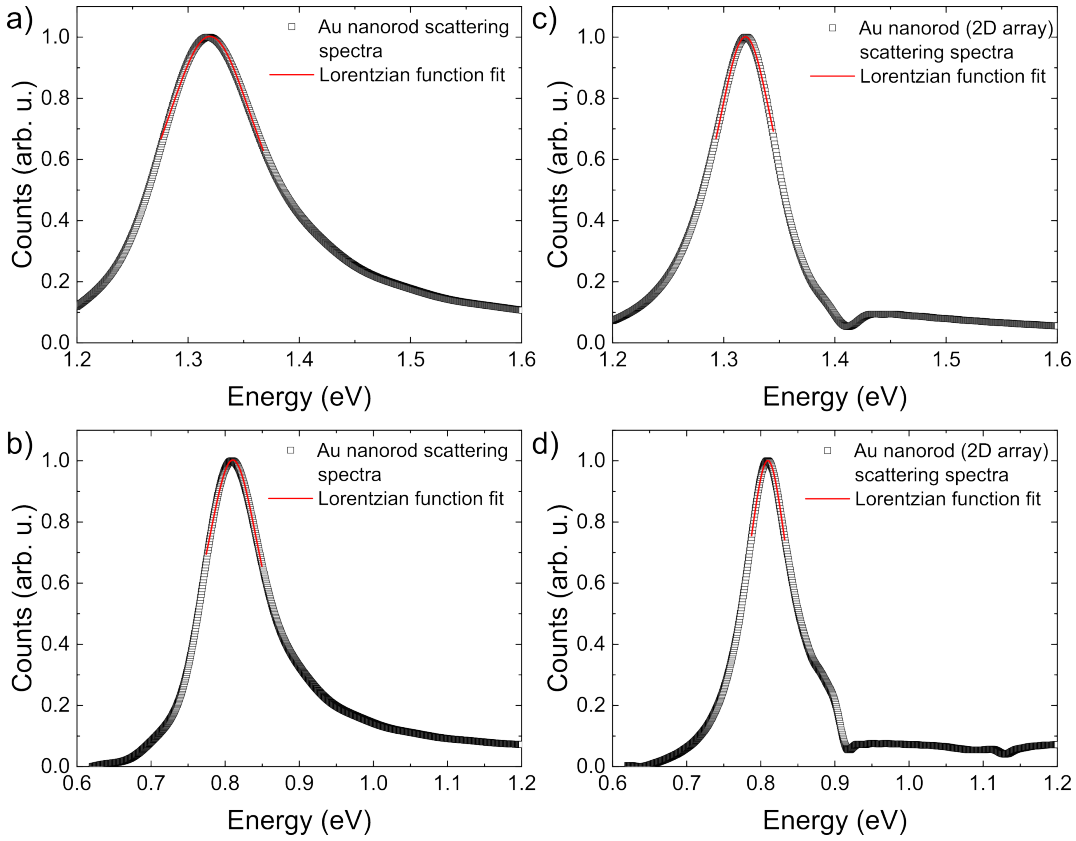

Figure S2. Scattering spectra of selected Au nanorods (black squares) together with Lorentzian fits (red lines). **a,b,** Scattering spectra of isolated nanorods with dimensions of (**a**) 130 nm (length, L) × 30 nm (diameter, D) and (**b**) 240 nm (L) × 30 nm (D). **c,d,** Scattering spectra of the same nanorods as in (**a**) and (**b**), respectively, arranged in a 2D periodic array with lattice constants of (**c**) 600 × 880 nm and (**d**) 980 × 1300 nm.

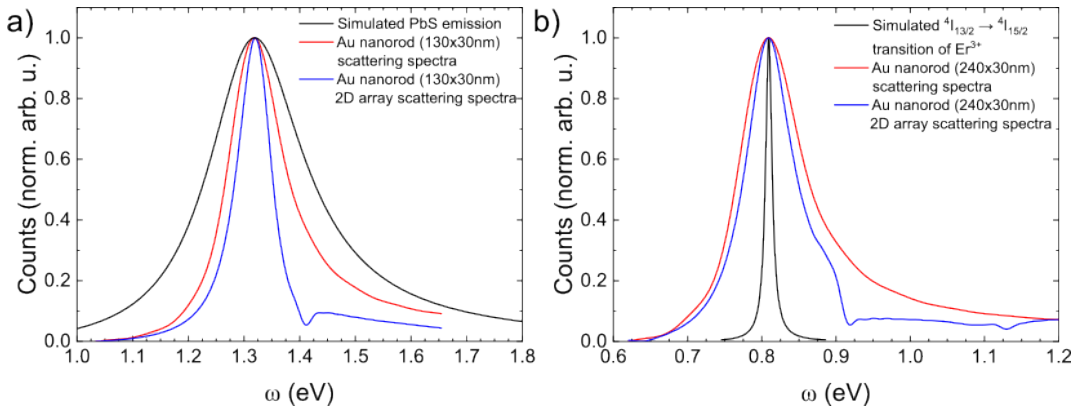

Figure S3. Spectral overlap between the selected emitters and the Au nanorod antennas used in the simulations. **a**, Simulated PbS emission spectrum (black) compared with the scattering spectra of a single Au nanorod (red) and a periodic 2D array of the same nanorods (blue). **b**, Simulated Er^{3+} $^4I_{13/2} \rightarrow {}^4I_{15/2}$ emission band (black) compared with the scattering spectra of a single Au nanorod (red) and a periodic 2D array of the same nanorods (blue). The spectra illustrate the spectral matching conditions used to define broad- and narrow-band antenna for the wide-band and narrow-band emitter cases.

Parameter extraction

The parameters used in the quantum-optical simulations were derived from the experimentally motivated emitter properties and from the simulated scattering spectra of the Au nanorod antennas. The antenna resonance energy ω_c was taken as the energy of

the scattering maximum, while the antenna linewidth κ was identified with the full width at half maximum (FWHM) of the corresponding plasmonic resonance,

$$\kappa = \mathrm{FWHM_c}. \tag{S12}$$

The emitter transition energy ω_e was taken from the maximum of the corresponding model emission spectrum, and the spectral detuning between emitter and antenna was defined as

$$\Delta = |\omega_c - \omega_e|. \tag{S13}$$

The emitter radiative decay rate γ was estimated from the experimentally determined average emission decay time $\langle\tau\rangle$ using the energy-time relation

$$\gamma = \frac{\hbar}{\langle\tau\rangle}, \tag{S14}$$

with $\hbar = 0.658212$ meV ps and $\langle\tau\rangle$ expressed in ps. The pure dephasing rate γ_ϕ was then chosen so as to reproduce the experimental emitter linewidth within the present Lindblad formulation. For the collapse operators used in the model, the emitter coherence decays with the transverse relaxation rate

$$\Gamma = \frac{\gamma}{2} + \gamma_\phi. \tag{S15}$$

Accordingly, the homogeneous emitter linewidth is given by

$$\mathrm{FWHM_e} = 2\Gamma = \gamma + 2\gamma_\phi. \tag{S16}$$

Thus, for a given experimental emitter linewidth, the pure dephasing rate was obtained as

$$\gamma_\phi = \frac{\mathrm{FWHM_e} - \gamma}{2}. \tag{S17}$$

In the limit of long-lived emitters, where $\gamma \ll \mathrm{FWHM_{em}}$, this reduces to the approximate relation

$$\gamma_\phi \approx \frac{\mathrm{FWHM_e}}{2}. \tag{S18}$$

Therefore, in the present model, the antenna linewidth is introduced directly as $\kappa = \mathrm{FWHM_c}$, whereas the emitter linewidth is distributed between the radiative decay rate γ and the pure dephasing rate γ_ϕ according to the relations above.

Table S1. Parameters used in the quantum-optical simulations for the selected emitter-antenna systems. WBS corresponds to PbS and NBS to Lu_2O_3:Er^{3+}. The definitions of all quantities and the parameter-extraction procedure are given in the. The uncertainties in the extracted plasmonic parameters are below 5%.

Material	ω_c (eV)	κ (meV)	ω_e (eV)	γ_ϕ (meV)	$\langle\tau\rangle$ (μs)	γ (meV)	Δ (meV)
Au nanorod ($L = 130$ nm, $D = 30$ nm), single	1.320	125	1.319 (WBS)	75	4.2[6]	1.57×10^{-7}	1
Au nanorod ($L = 130$ nm, $D = 30$ nm), 2D array ($X = 600$ nm, $Y = 880$ nm)	1.320	75.1	1.319 (WBS)	75	4.2[6]	1.57×10^{-7}	1
Au nanorod ($L = 240$ nm, $D = 30$ nm), single	0.810	108	0.809 (NBS)	9.9	0.6[7]	1.1×10^{-9}	1
Au nanorod ($L = 240$ nm, $D = 30$ nm), 2D array ($X = 980$ nm, $Y = 1300$ nm)	0.809	77.1	0.809 (NBS)	9.9	0.6[7]	1.1×10^{-9}	1

Detuning-dependent evolution of the detected emission spectra

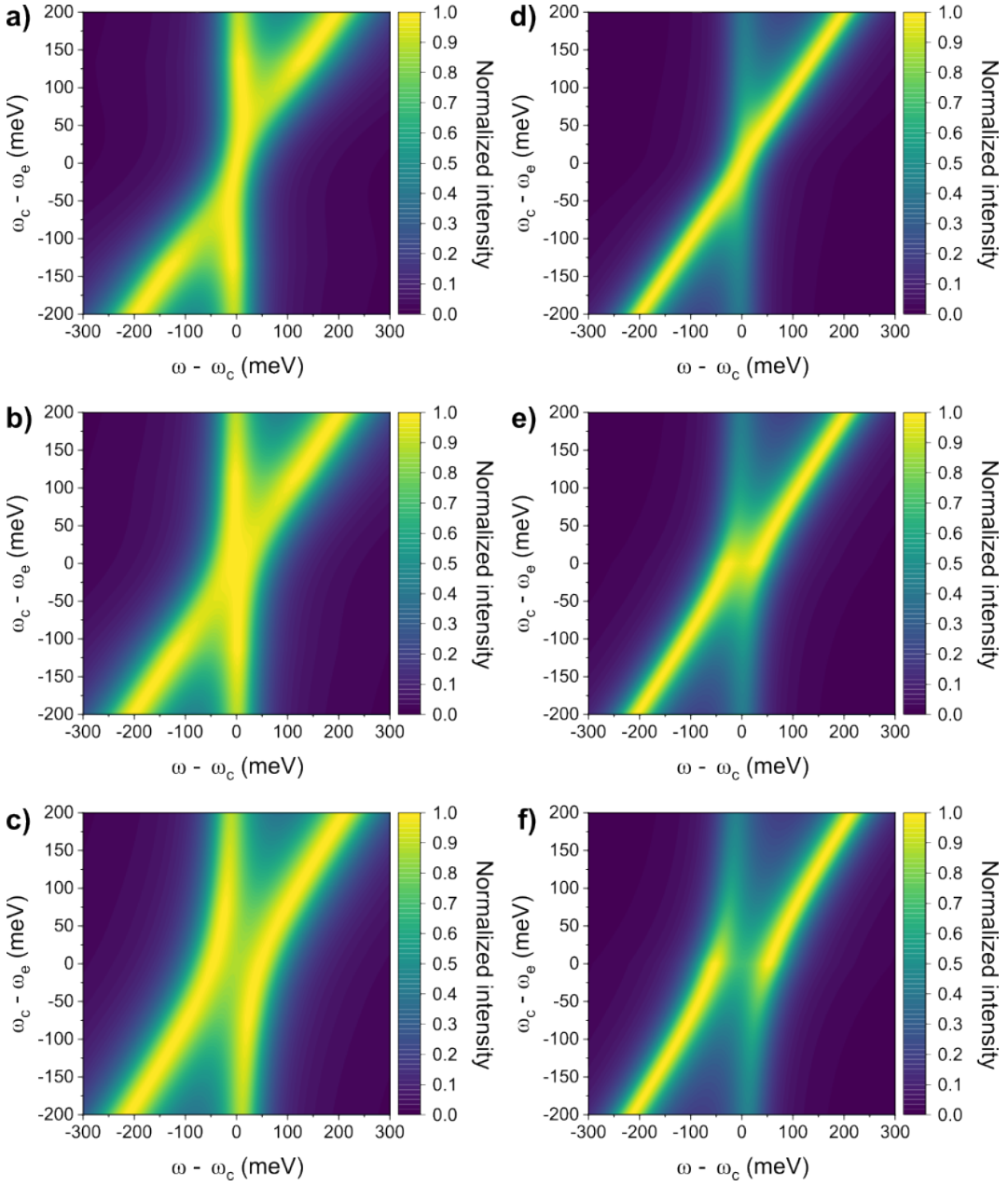

Figure S4. Normalized spectral maps of the detected emission S_{det} for a wide-band scintillator (WBS) coupled to Au nanorods, plotted as a function of emission energy $(\omega - \omega_c)$ and detuning $(\omega_c - \omega_e)$. Panels (a,b,c) show the wider-band antenna, and panels (d,e,f) show the narrower-band antenna. The coupling strength is $g = 20$ meV in (a,d), $g = 40$ meV in (b,e), and $g = 60$ meV in (c,f). Each spectrum was normalized independently to highlight the evolution of the spectral shape. The onset of anticrossing becomes more evident with increasing g and is more clearly resolved for the narrower-band antenna.

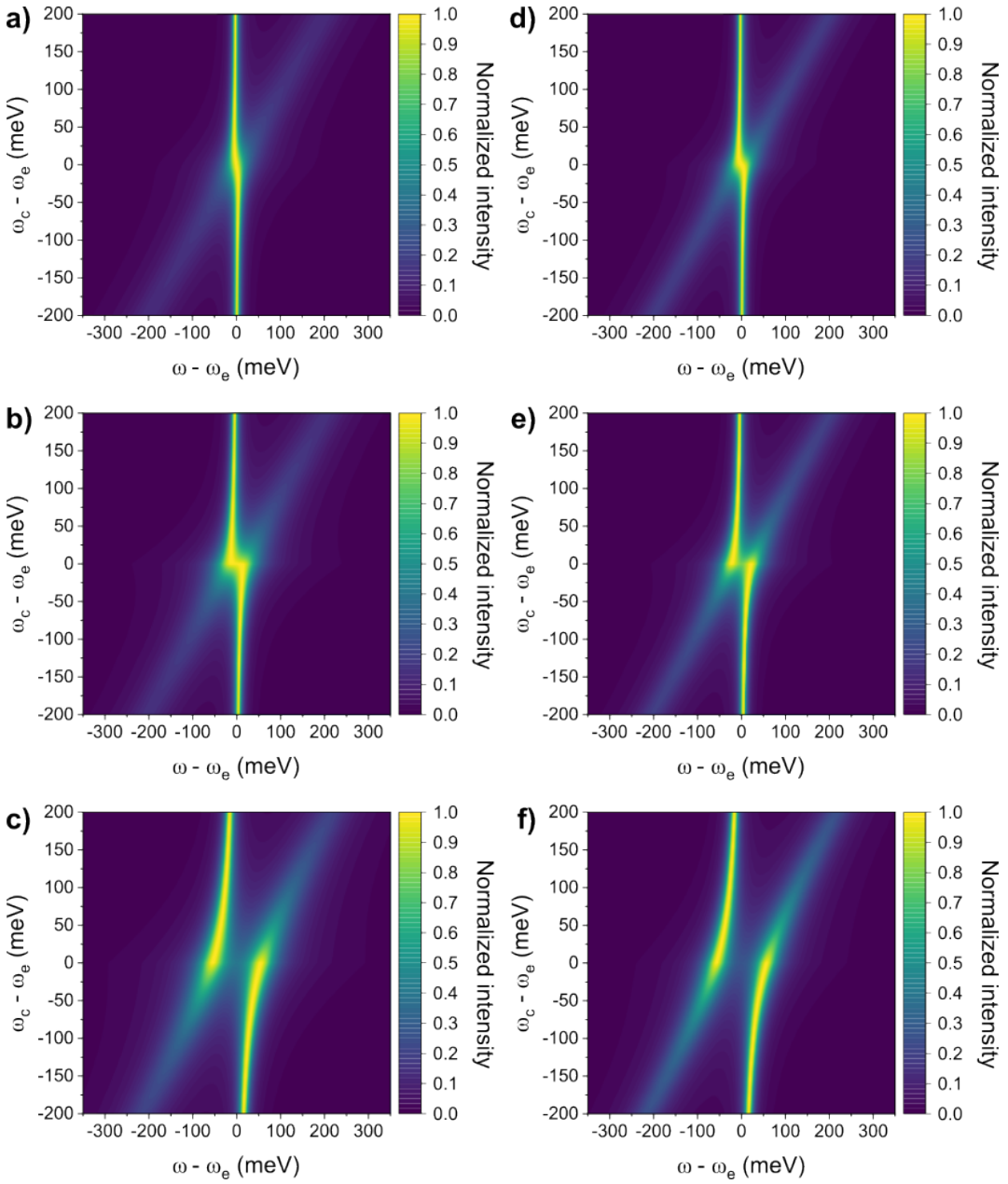

Figure S5. Normalized spectral maps of the detected emission S_{det} for a narrow-band scintillator (NBS) coupled to Au nanorods, plotted as a function of emission energy $(\omega - \omega_c)$ and detuning $(\omega_c - \omega_e)$. Panels (a,b,c) show the wider-band antenna, and panels (d,e,f) show the narrower-band antenna. The coupling strength is $g = 20$ meV in (a,d), $g = 40$ meV in (b,e), and $g = 60$ meV in (c,f). Each spectrum was normalized independently to highlight the evolution of the spectral shape. The onset of anticrossing becomes more evident with increasing g and is more clearly resolved for the narrower-band antenna.

1 Calculation of temporal decay traces

The general quantum-optical model, parameter extraction, and numerical implementation are described above. Here, we summarize only the procedure used to calculate the transient decay traces and the corresponding effective Purcell-type enhancement factors.

To simulate the decay dynamics, the emitter-antenna system was initialized in a prepared state with the emitter excited and the cavity mode empty,

$$|\psi(0)\rangle = |e,0\rangle. \tag{S19}$$

In this transient branch of the calculation, the incoherent pumping terms were set to zero, so that only cavity loss, emitter decay, and pure dephasing were retained.

The subsequent time evolution was obtained from the same Lindblad master equation as used for the steady-state calculations. From the time-dependent density matrix, we evaluated the emitter population

$$n_{\mathrm{emit}}(t) = \langle \hat{\sigma}^{\dagger}\hat{\sigma}\rangle_t \tag{S20}$$

and the cavity population

$$n_{\mathrm{cav}}(t) = \langle \hat{a}^{\dagger}\hat{a}\rangle_t. \tag{S21}$$

To quantify the effective decay rate, the transient emitter population was fitted with a single-exponential function,

$$n_{\mathrm{emit}}(t) = A\exp[-\Gamma(g)t], \tag{S22}$$

where A is the fitted amplitude and $\Gamma(g)$ is the effective decay rate obtained for a given coupling strength g. The fit was applied only after a short initial time cutoff and only over the range where the emitter population remained above a fixed fraction of its maximum value, in order to avoid numerical artifacts at very short times and low-signal tails at late times.

The Purcell-type enhancement values reported in this work were then obtained by normalizing the fitted decay rates to the value calculated at the lowest considered coupling strength, $g = 1$ meV,

$$F_{\mathrm{P}}(g) = \frac{\Gamma(g)}{\Gamma(1\ \mathrm{meV})}. \tag{S23}$$

This reference was used instead of the bare radiative rate $\gamma/\hbar$, because the latter is extremely small for the long-lived emitters considered here and would therefore lead to unrealistically large enhancement factors. Using $\Gamma(1\ \mathrm{meV})$ as the reference provides a more conservative, physically meaningful estimate of the transient decay acceleration within the same modeling framework.

Within the weak-coupling regime, F_{P} can be interpreted as an effective Purcell-type enhancement of the emitter decay dynamics. At larger coupling strengths, where hybrid light-matter states begin to form, and the dynamics may deviate from a strictly irreversible spontaneous-emission picture, it should be understood more generally as a fitted temporal acceleration factor. We define the intermediate-coupling region for g values at which the decay behavior ceases to be exponential. Obtained F_{P} are summarized in Fig. S6

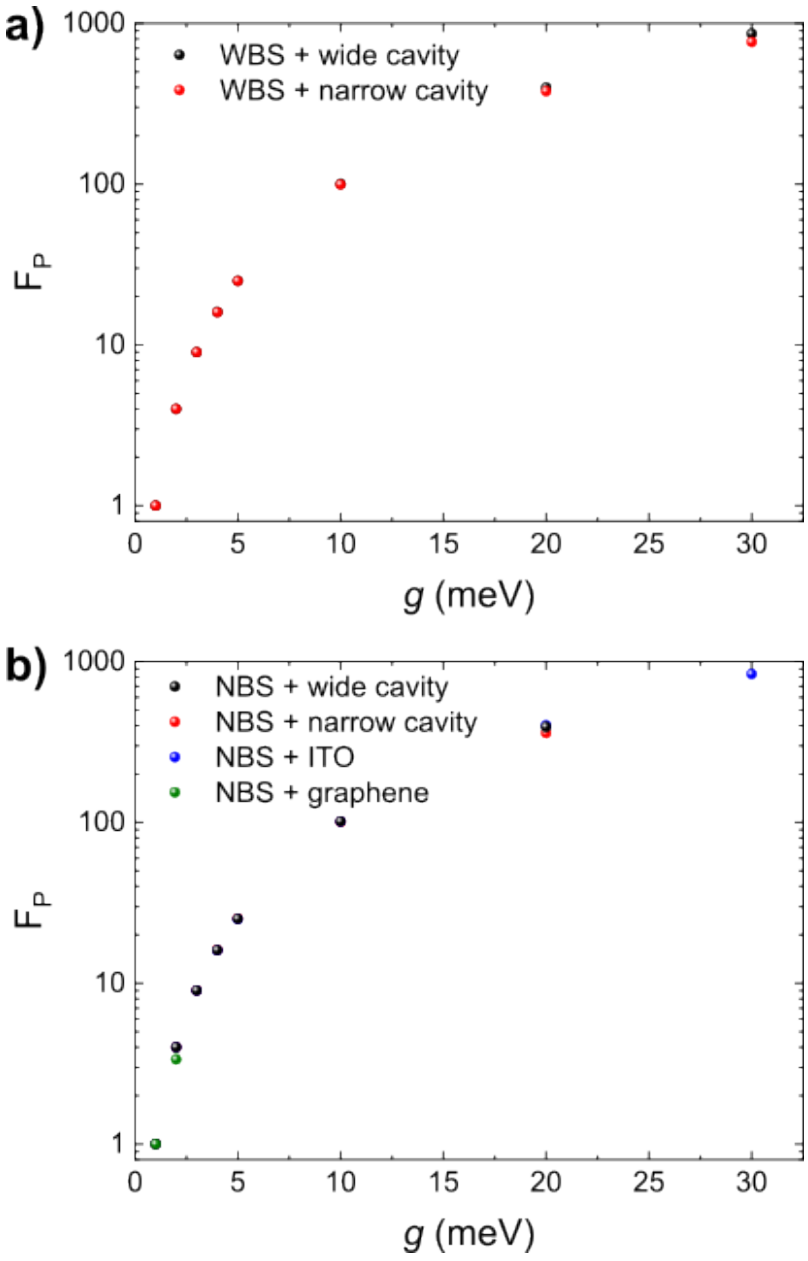

Figure S6. Calculated Purcell factors for WBS (a) and NBS (b).

Alternative antennas

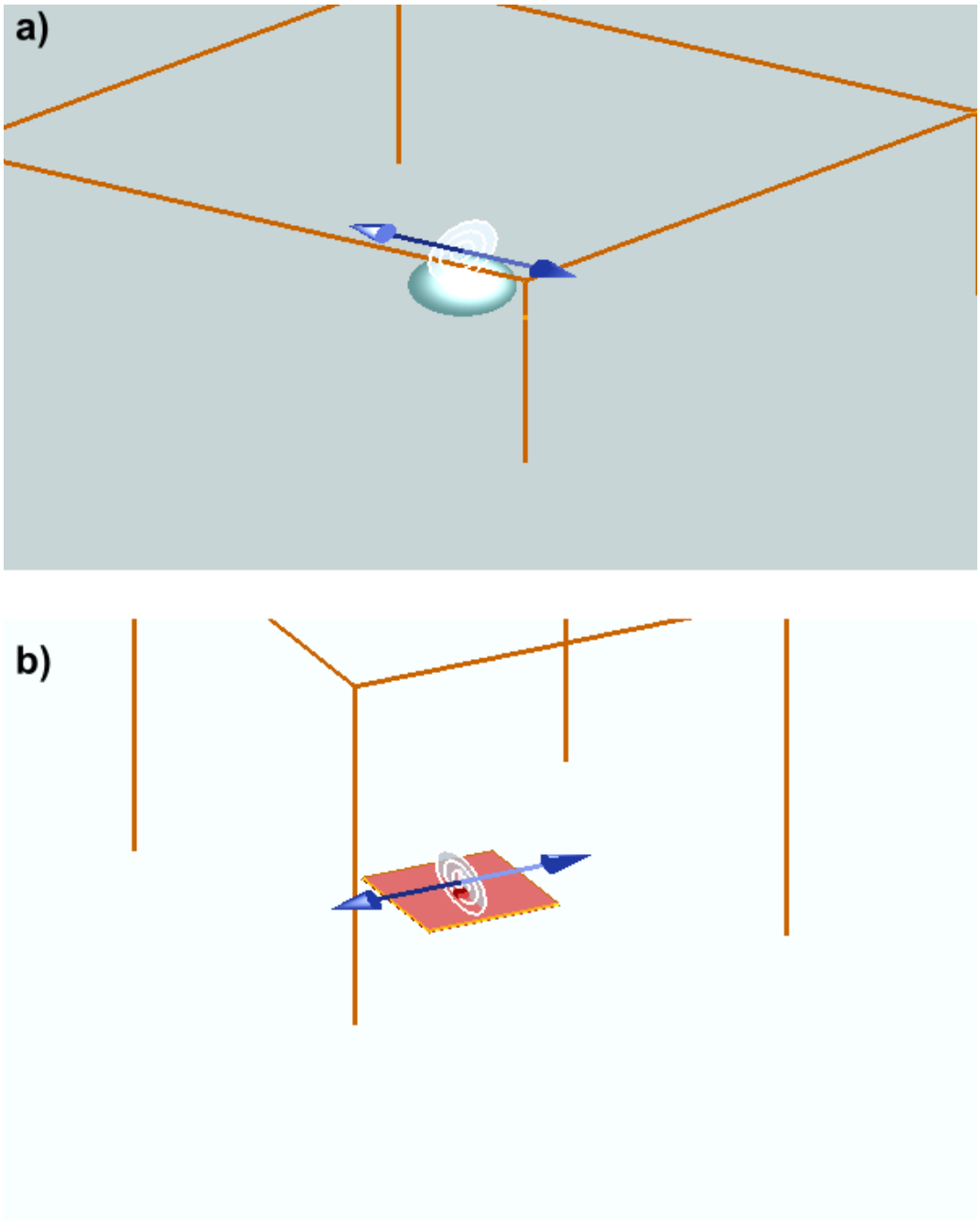

Figure S7. Schematic representation of the simulated ITO (a) and graphene (b) structures and excitation geometry

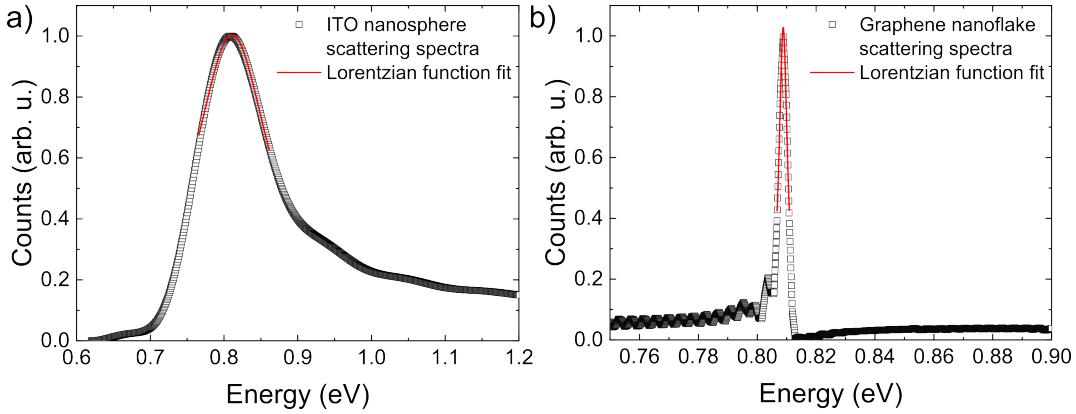

Figure S8. Scattering spectra of selected alternative antennas (black squares) together with Lorentzian fits (red lines). **a,** Scattering spectra of isolated ITO nanosphere ($r = 45$ nm). **b,** Scattering spectra of graphene nanoflake (13×13 nm and thickness of 1 nm)

Table S2. Parameters used in the quantum-optical simulations for the selected alternative antennas. The definitions of all quantities and the parameter-extraction procedure are given in the. The uncertainties in the extracted plasmonic parameters are below 5%.

Material	ω_c (eV)	κ (meV)	ω_e (eV)	γ_ϕ (meV)	$\langle\tau\rangle$ (μs)	γ (meV)	Δ (meV)
ITO nanosphere ($r = 45$ nm)	0.810	129	0.809 (NBS)	9.9	0.6[7]	1.1×10^{-9}	1
Graphene nanoflake (13×13 nm and thickness of 1 nm)	0.809	3.5	0.809 (NBS)	9.9	0.6[7]	1.1×10^{-9}	0

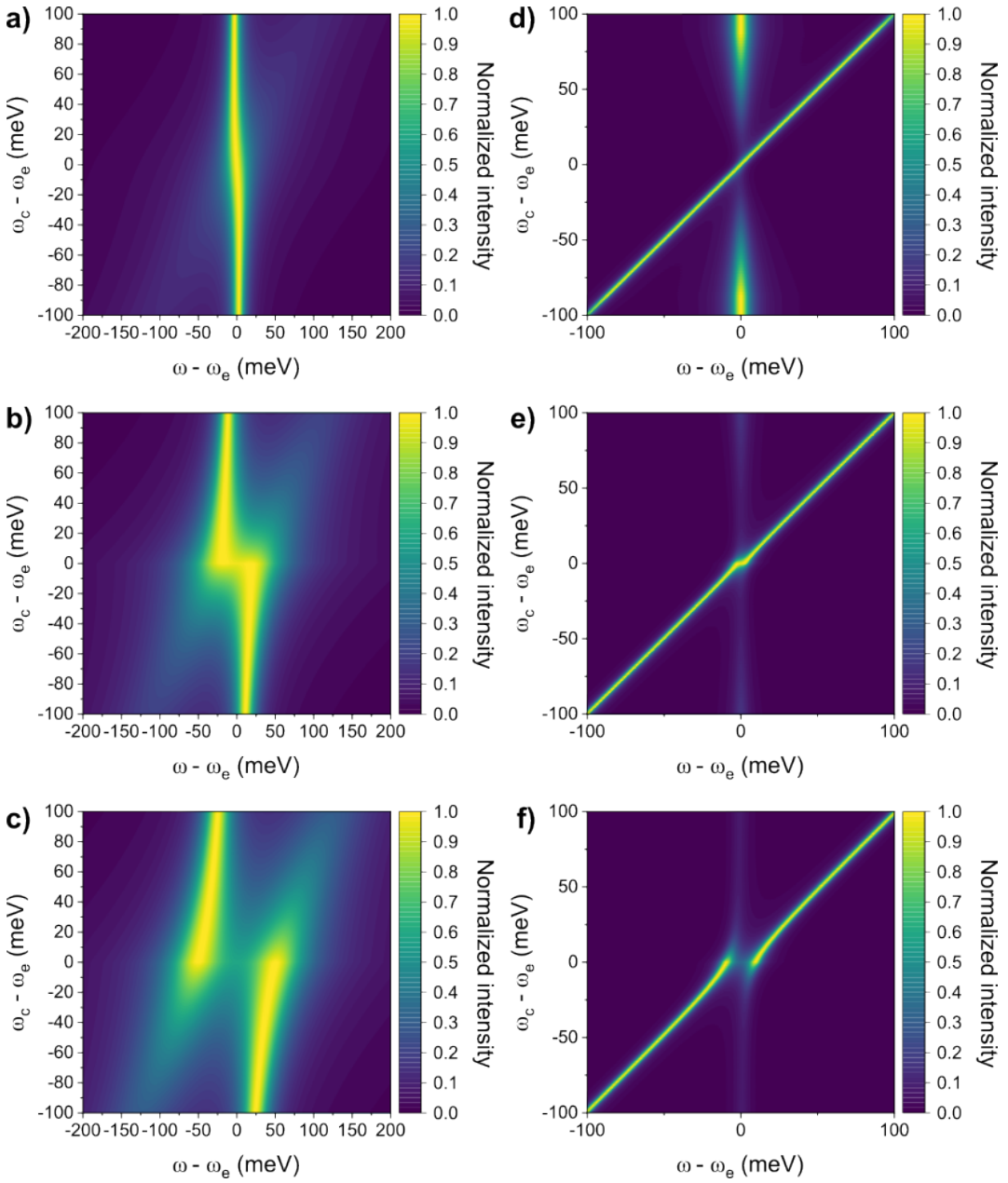

Figure S9. Normalized spectral maps of the detected emission S_{det} for a narrow-band scintillator (NBS) coupled to alternative antennas, plotted as a function of emission energy $(\omega - \omega_c)$ and detuning $(\omega_c - \omega_e)$. Panels (a,b,c) show the ITO antenna, and panels (d,e,f) show the graphene antenna. The coupling strength is $g = 20$ meV in (a), $g = 40$ meV in (b), and $g = 60$ meV in (c) while $g = 1$ meV in (d), $g = 4$ meV in (e), and $g = 10$ meV in (f). Each spectrum was normalized independently to highlight the evolution of the spectral shape.

References

1. Breuer, H. P. & Petruccione, F. The theory of open quantum systems. *Oxf. Univ. Press.* (2007).
2. Carmichael, H. An open systems approach to quantum optics. *Springer* (1993).
3. Jaynes, E. T. & Cummings, F. W. Comparison of quantum and semiclassical radiation theories with application to the beam maser. *Proc. IEEE* **51**, 89–109, DOI: 10.1109/PROC.1963.1664 (1963).
4. Johansson, J. R., Nation, P. D. & Nori, F. Qutip: An open-source python framework for the dynamics of open quantum systems. *Comput. Phys. Commun.* **183**, 1760–1772, DOI: 10.1016/j.cpc.2012.02.021 (2012).
5. Johansson, J. R., Nation, P. D. & Nori, F. Qutip 2: A python framework for the dynamics of open quantum systems. *Comput. Phys. Commun.* **184**, 1234–1240, DOI: 10.1016/j.cpc.2012.11.019 (2013).
6. Grevtseva, I. *et al.* Size effect features and mechanism of luminescence of colloidal pbs quantum dots, passivated with thioglycolic acid. *Opt. Quantum Electron.* **55**, 433, DOI: 10.1007/s11082-023-04658-3 (2023).
7. Avram, D., Tiseanu, I., Vasile, B. S., Florea, M. & Tiseanu, C. Near infrared emission properties of er doped cubic sesquioxides in the second/third biological windows. *Sci. Reports* **8**, 18033, DOI: 10.1038/s41598-018-36639-y (2018).